

# Chapter 8

## Honeycomb Burner Model



**Figure 8.1:** Side-on photograph of honeycomb burner flame

## 8.1 Purpose of the Honeycomb Burner Model

The purpose of the honeycomb burner model is to indirectly establish the correct formation path for  $\text{OH}^*$  chemiluminescence. The honeycomb burner experimental setup provides a relatively simple 1-D flame environment that can be more easily modeled in its entirety than the more complicated 2-D structure of the Bunsen type flame. A side-on view of the flat flame on the honeycomb is shown in Figure 8.1. The 1-D environment takes many fluid-mechanical modeling uncertainties out of the scope of consideration and allows the model to focus on thermal and reactive interactions among the modeling components.

## 8.2 Honeycomb model derivation and description

To simplify the modeling of the honeycomb burner, only one square chamber is modeled with its associated part of the wall (half of the total wall thickness), as shown in Figure 8.2. A major assumption of the model is that there are no radial gradients in any quantity and that the flame is purely 1-D. The model will allow for axial area-change, as the gas exits from the honeycomb.

### 8.2.1 Heat balance for the fluid

The heat balance for the gas is illustrated in Figure 8.3. The element shown lies within the honeycomb, because convective heat-loss is to the honeycomb. The heat balance accounts for conduction and advection in and out of the differential volume element of area  $A$  and thickness  $dx$ . The heat balance also includes losses due to

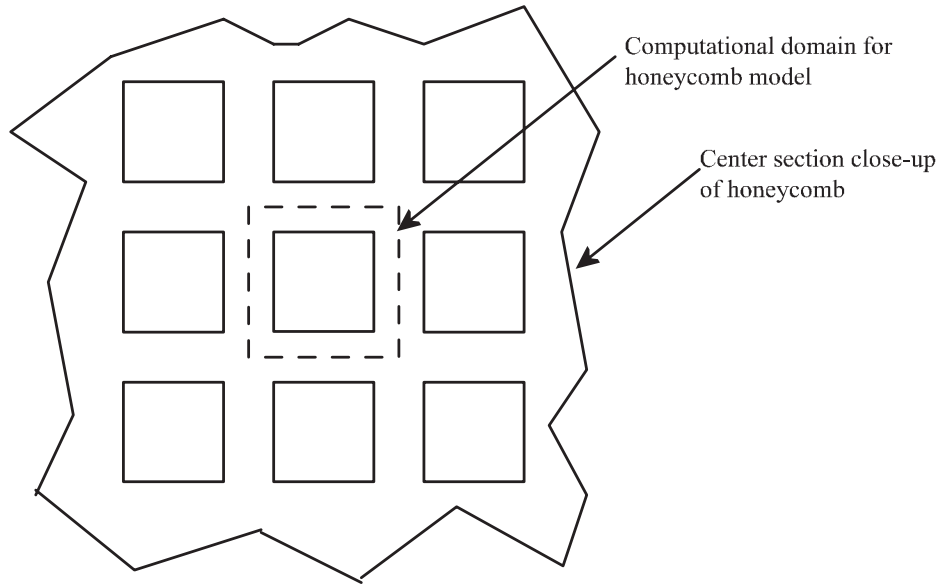


**Figure 8.2:** Schematic illustrating honeycomb computational domain

convection and radiation. Depending on the element, convective heat losses will be to the honeycomb for elements inside the honeycomb channel and to the surroundings outside the honeycomb channel. Convective heat-loss modeling is discussed in Section 8.2.3. Radiative heat-loss from the gas is to the surroundings and the honeycomb walls. The exact distribution of how much radiation is lost to the surroundings and how much is lost to the honeycomb walls depends on the physical location of the gas element under consideration as described in Section 8.2.3. The equation resulting from the heat balance shown in Figure 8.3 is given in Equation 8.1. Note that the equation omits the thermal diffusion and chemical reaction energy source terms. In the end, the equation solved will be identical to the equation shown in Equation 6.3. The present development illustrates the origin of some of the terms in Equation 6.3 and more explicitly shows how the heat-loss terms enter the equation. The heat balance also shows how the honeycomb solid temperatures are coupled to the gas temperatures.

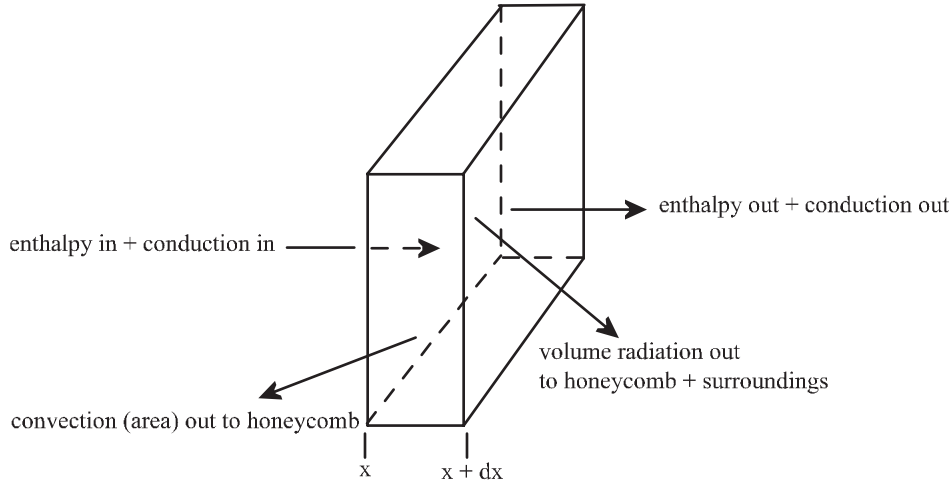


**Figure 8.3:** Schematic illustrating honeycomb gas heat balance

$$\dot{M} \frac{\partial T_{gas}}{\partial x} - \frac{1}{c_p} \frac{\partial}{\partial x} \left( \lambda A \frac{\partial T_{gas}}{\partial x} \right) + \frac{P}{c_p} \left( h_{conv} (T_{gas} - T_{hc}) \right) + \frac{Q'_{rad-loss}}{c_p} = 0 \quad (8.1)$$

Equation 8.1 is discretized for variable grid-spacing as given in the PREMIX manual (Kee et al., 1993). The discretization used exhibits second order accuracy using central differencing. The derivatives of the product terms are calculated by first calculating the product terms and then calculating a central difference to obtain the local derivative of the quantity.

The boundary conditions for the gas are a constant temperature at the honeycomb inlet. Except for reactant species, all species concentrations are also set to zero at the inlet to the honeycomb burner. Reactant species have a specified mole-fraction at the inlet. At the downstream end, a surface boundary condition is specified with radiative heat-loss but without advection or convection, since the boundary condition is of the surface type. The downstream boundary condition is given symbolically in Equation 8.2. The discretization of the downstream boundary condition is straight-

forward using an up-wind first order differencing formula.

$$A \lambda \frac{\partial T_{gas}}{\partial x} + Q_{rad-loss} = 0 \quad (8.2)$$

## 8.2.2 Heat balance for the honeycomb solid

The complete heat balance for the honeycomb solid is shown in Figure 8.4. The corresponding equation for the honeycomb solid is given in Equation 8.3. The area  $A$  in the case of the honeycomb solid refers to the honeycomb cross-sectional area, not the flow cross-sectional area. It is also important to realize that the radiation term in this case is not merely a loss term but includes an incoming component from the gas as well. The details of the radiation model will be discussed in Section 8.2.3. The discretization of Equation 8.3 is second order accurate using central differences, similar to the discretization used for the gas.

$$\lambda \frac{\partial^2 T_{hc}}{\partial x^2} + \frac{P}{A} \left( h_{conv} (T_{gas} - T_{hc}) \right) + \frac{Q'_{rad-in}}{A} = 0 \quad (8.3)$$

The boundary condition for the honeycomb burner temperature at the inlet is a surface heat balance among the radiation loss from the surface and the conduction into the surface from inside the honeycomb. At the honeycomb exit, a similar surface heat balance boundary condition is used. The first order differential equation representing the honeycomb exit boundary condition is given in Equation 8.4. The boundary condition at the honeycomb entrance has the exact same form with the lone difference that a minus sign must be added in front of the conduction term. The discretization is straight-forward using first-order accurate finite difference expressions.

$$A \lambda \frac{\partial T}{\partial x} - Q_{rad-in} = 0 \quad (8.4)$$

## 8.2.3 Heat-transfer in the honeycomb burner model

### Convective heat-transfer

The convective heat-transfer that must be modeled is the convective heat-transfer between the honeycomb wall and the gas inside the honeycomb channel and convective heat-transfer outside the honeycomb channel between the gas and the quartz

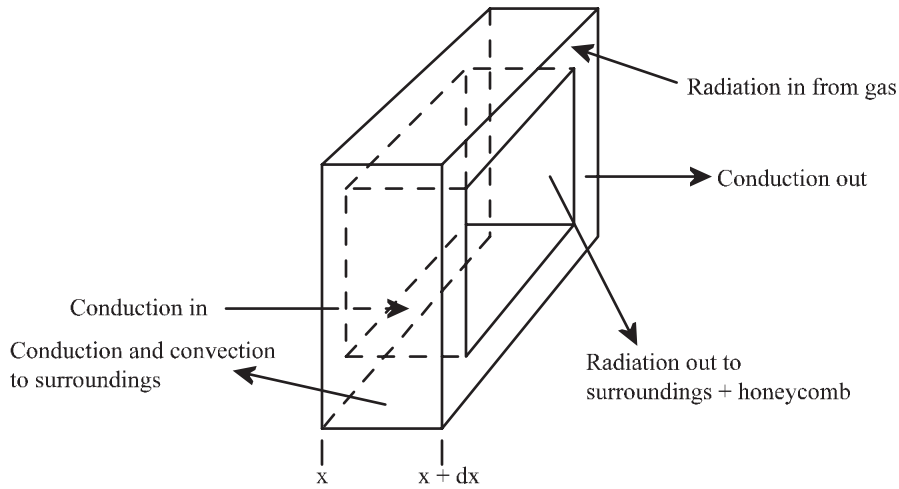


**Figure 8.4:** Schematic illustrating honeycomb solid material heat balance

tube. The heat-transfer between the honeycomb and the gas is modeled by assuming a constant Nusselt number of 3.5, as given in Kreith and Bohn (1993) . The heat-transfer coefficient is then calculated based on the local value of the mean conductivity of the gas and the honeycomb channel width. The resulting heat-transfer coefficient lies between 30 and 100 W/(m<sup>2</sup> °K). Outside the honeycomb channel modeling non-radiative heat-loss is more difficult. Radial heat-transfer may be significant and must be included in the model for it to be complete. To account for this effect the heat-loss is calculated by assuming that the flame temperature does not vary radially and that the heat is extracted uniformly from all of the fluid along one axial station. To model the heat-loss, the heat-transfer from the gas to the surroundings has to be specified. The convective heat-transfer coefficient from the gas to the quartz chimney is set to 30 W/(m<sup>2</sup> °K). There is no radiative transfer to the quartz tube since radiative heat-loss is accounted for separately. The quartz chimney is assumed to have a conductivity of 1.07 W/(m °K) and an emissivity to the surroundings of 0.93. The natural convection heat-transfer coefficient on the outside of the quartz chimney is

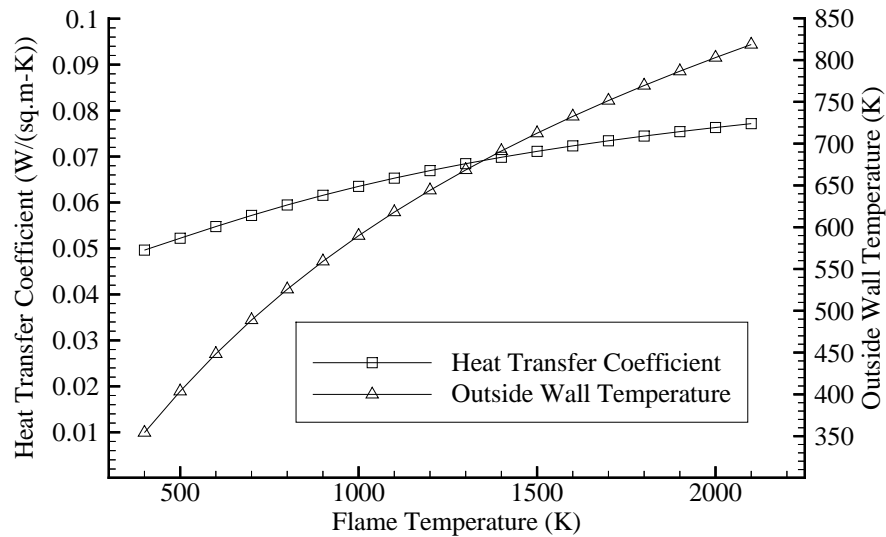


**Figure 8.5:** Volumetric heat-loss and chimney outside wall temperature as a function of flame temperature

set to  $12 \text{ W}/(\text{m}^2 \text{ }^\circ\text{K})$ . Figure 8.5 shows how the resulting effective heat-transfer coefficient varies with flame temperature. The low values indicate that the heat-transfer is relatively low but the convective heat-loss calculated may still significantly affect the temperature profile, especially if the convective heat-loss is on same order as the radiative heat-loss.

### Radiative heat-transfer

Calculating the radiative heat-transfer in the honeycomb burner model is very important to the physical veracity of the model. In experiments, significant honeycomb radiation is observed, indicating a very high honeycomb temperature caused by the radiative heat-transfer from the hot post-flame gases to the honeycomb solid. The difficulty in modeling radiative heat-transfer lies in the fact that the radiation from the flame gases is diffuse and radiates in all directions. Added to that is the problem that different parts of the honeycomb channel are exposed to different amounts of incoming radiation. Furthermore, different honeycomb parts exchange radiation.

The first simplifying assumption made is that the flame gases behave optically

thin and do not absorb or reflect any radiation. The radiation from the gas is modeled using the Planck mean absorption coefficient. Planck mean absorption coefficients for the dominant radiating species in combustion are taken from Yu et al. (1985). The volumetric heat-loss by radiation to surroundings at a temperature of  $T_s$  is given in Equation 8.5. The problem in determining the heat-loss is that the radiation target is not at a uniform temperature. Some of the radiation will be to the surroundings but part of the radiation will be to the honeycomb.

$$q''' = \sigma a_p (T - T_s) \quad (8.5)$$

The fact that the radiation target is not at a uniform temperature is usually handled by calculating area factors or view factors that account for what fraction of the total rays emitted reaches a given part of the radiation target. To calculate the radiation heat-loss, each radiating volume, given by the differential element shown in Figure 8.3 is considered to radiate through each of the element's faces according to that face's area compared to the total surface area of the differential element. If the differential element were a cube, this would mean that 1/6 of the rays will travel through each of the faces. For differential gas elements inside the honeycomb channel, radiation out from the sides of the differential element is radiated directly to the honeycomb channel wall. For this part of the radiation, an area factor of 1 will be used. The net radiation heat-transfer is then determined by the temperature difference between the differential gas element and the corresponding differential solid honeycomb element.

Calculation of the view factor becomes more difficult when the radiation from the gas element inside the honeycomb channel through a face that is perpendicular to the flow is considered. The area factor then depends greatly on the relative position of the participating elements. To calculate the view factor among elements whenever the value isn't possible to be determined by inspection, a formula given in Hottel (1967) is used. The formula is shown in Equation 8.6. The double contour integral is relatively easy to evaluate given that the participating elements are always either perpendicular or parallel to each other.

$$F_{12} = \frac{1}{2\pi} \oint_2 \oint_1 \ln(r) \cos(\theta) dl_1 dl_2 \quad (8.6)$$

Area factors are calculated for radiative transfer inside the honeycomb channel from gas to honeycomb elements. Radiative transfer among the honeycomb elements is ignored. Area factors are calculated for radiation from the honeycomb to the surroundings. Area factors are also calculated for radiation into the honeycomb from gases outside the honeycomb. The area factors calculated are based on the presence of a flame sheet much larger than the width of the honeycomb channel, i.e. the modeled honeycomb channel element receives radiation not only from the modeled flame gases but from the entire flame-sheet as it would exist in the experiment, assuming a uniform radial temperature equal to the modeled gas temperature at the same axial location. The modeling calculations are performed using an average amount of incoming radiation. The center of the honeycomb is exposed to the highest radiation, whereas the outer part of the honeycomb is exposed to the least amount of radiation. However, all of the honeycomb surface receives radiation from areas of the flame not directly above a particular honeycomb cell. The radiation model would be grossly inaccurate if the added radiation input from the rest of the flame were not accounted for in some way. To obtain an average incoming radiation, a view factor from the entire flame-sheet area to the entire honeycomb burner surface area is calculated. The calculation uses representative square areas to avoid the difficulty of calculating the contour integral of Equation 8.6 for circular areas. The calculated area-factor is then used in reference only to the modeled part of the surface. The area-factor used is much smaller than the area-factor one would calculate by assuming that the modeled honeycomb chamber lies in the center of the honeycomb burner surface. The area factor is also larger than the area factor calculated between simply the modeled flame element and the modeled honeycomb surface. Assuming the center location for the modeled honeycomb cell may model the actual center honeycomb cell well, but the calculated heat transfer would not be representative of the actual average heat-transfer occurring.

The average area factor between a gas layer and the honeycomb surface is shown as a function of the distance between the gas layer and the burner surface in Figure 8.6. The area factor from the exit area of the honeycomb channel to the honeycomb

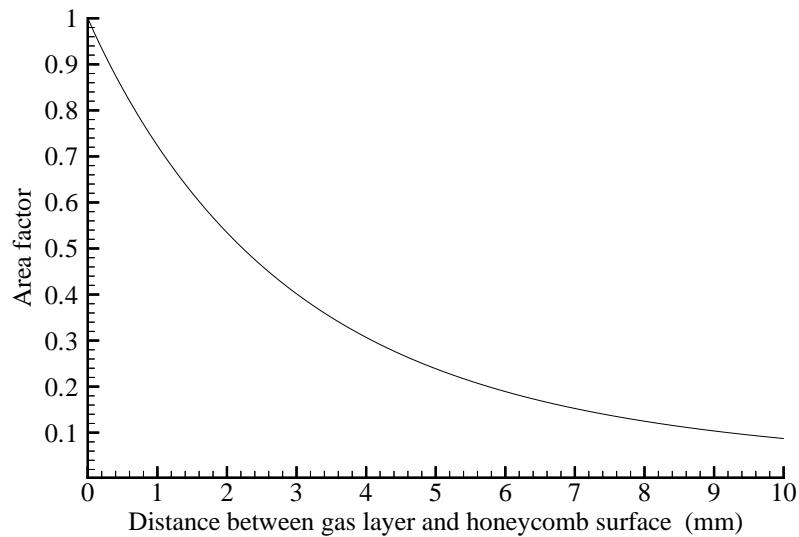


**Figure 8.6:** Area factor governing radiation exchange between a gas layer and the honeycomb surface

elements along the honeycomb channel itself is shown in Figure 8.7 as a function of the distance from the honeycomb exit. All of the area factors shown are in reference to the receiving area, not the emitting area.

Accounting for the variation of temperature in the radiation target, an expression for the radiation loss per unit length of any gas element using view factors is shown in Equation 8.7. The first part of the equation calculates the amount of radiation lost to the honeycomb. The second part of the equation calculates what fraction of the rays is left to radiate to the surroundings and the amount of associated heat-loss. Similar equations may be written for the honeycomb elements, where care must be taken to calculate the net radiation heat-transfer, not only the out-going radiation

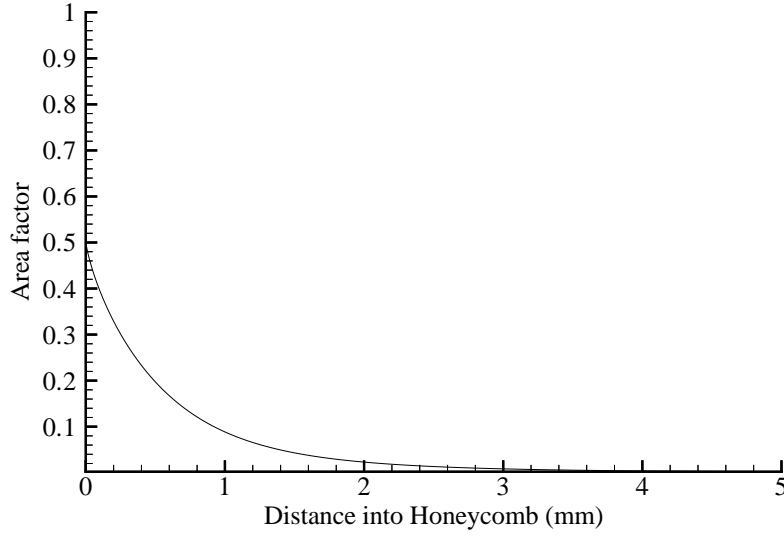


**Figure 8.7:** Area factor governing radiation exchange between honeycomb surface and the interior honeycomb sides

component.

$$\begin{aligned}
 Q'_{rad-loss} = a_p \sigma A_{local} & \left\{ \frac{A_{local}}{2 A_{local} + 4 \sqrt{A_{local}} \Delta x} \right. \\
 & \left( F_{local \rightarrow surf} (T_{local}^4 - T_{surf}^4) + F_{local \rightarrow 0} \sum_{i=1}^N F_{0 \rightarrow i} (T_{local}^4 - \epsilon_{hc} T_i^4) \right) \\
 & + \left[ 1 - \left( F_{local \rightarrow surf} + F_{local \rightarrow 0} \sum_{i=1}^N F_{0 \rightarrow i} \right) \right. \\
 & \left. \left. \frac{A_{local}}{2 A_{local} + 4 \sqrt{A_{local}} \Delta x} \right] (T_{local}^4 - T_s^4) \right\}
 \end{aligned} \tag{8.7}$$

The radiating surface boundary condition used for the gas at the downstream end of the computational domain is difficult to specify because radiation from the gas is generally a volume process. In effect, the slope in temperature at the end of the computational domain must supply an amount of heat equal to the local heat-loss per unit axial length. If one imagined an infinitely large element added on to the true computational domain, an average rate of heat-loss per unit axial length may be calculated by performing a limit calculation as shown in Equation 8.8. The temperature

of the imagined element is set equal to the boundary temperature. The calculations showed that the choice of the temperature does not affect results significantly since the computational domain is large enough to essentially de-couple the boundary condition from the actual domain of interest near the exit of the honeycomb.

$$\begin{aligned}
 Q'_{rad-loss} &= \lim_{\Delta x \rightarrow \infty} \left( a_p \sigma A_{surf} \Delta x \frac{A_{surf}}{2 A_{surf} + 4 \sqrt{A_{surf} \Delta x}} \right) \\
 &= \frac{a_p \sigma}{4} A_{surf}^{\frac{3}{2}}
 \end{aligned} \tag{8.8}$$

### 8.3 Honeycomb modeling procedure

The honeycomb model as described in Section 8.2 is incorporated into the existing PREMIX code. The honeycomb temperature variable is added to the solution array. The original structure of the PREMIX code requires that the Jacobian matrix has a banded structure. Due to the radiation coupling, the banded structure no longer exists. As written, the code neglects the off-diagonal terms of the Jacobian but the solution stability is not affected by the simplification.

In order to solve a honeycomb burner problem, a conventional PREMIX burner stabilized flame problem is solved first with the origin of the computational domain located at  $x = 0$  cm. In the end, the  $x = 0$  point will represent the top of the honeycomb burner. The solution of the burner stabilized flame problem allows the species profiles to be established before true honeycomb temperature calculations begin. When given the keyword 'HOCO', PREMIX calls an initialization routine that adds the honeycomb to the computational domain. The grid spacing varies smoothly from 0.015 cm near the exit of the honeycomb to 0.03 cm at the entrance of the honeycomb.

The initialization routine also calculates the honeycomb and gas temperatures inside the honeycomb channel based on the temperatures calculated outside the honeycomb. The routine serves to give a good starting guess at the temperatures back to the PREMIX program. PREMIX then attempts solution of the full honeycomb model equations by the same method used for all other PREMIX modeling calculations.

The resolution of the final solution is very high, using at least 450 points in every case. The continuation feature of PREMIX is used in the calculation of all the cases studied to use CPU time more efficiently. The continuation feature allows previous modeling results to be used as the initial guess for another modeling calculation with slightly different parameters. The variation of equivalence ratio for each of the flow-rates is accomplished in this way. For example, the solution at an equivalence ratio of 0.6 serves as the initial condition for the calculation at an equivalence ratio 0.625.

## 8.4 Honeycomb Modeling Results

The modeling results will cover the comparison of chemiluminescence modeling results with experimental data first to establish the most accurate mechanism. All other results shown will then be based on the most accurate mechanism as determined by the mechanism's ability to match experimental chemiluminescence trends.

### 8.4.1 Comparison with experimental data

As discussed in Section 6.2, two mechanisms for OH\* chemiluminescence formation are tested using a comparison between modeling results and experimental data. The first formation path is the traditionally accepted formation path through CH as given in Equation 1.1. The second formation path tested is that through the formyl radical, as given by Equation 6.5.

Similar to the Bunsen burner model comparisons with experimental data, a conversion factor from experimental units to modeling units is required. To determine the constant, the following procedure is used. Ratios of the OH\* chemiluminescence modeling results to the OH\* chemiluminescence experimental data are taken for all experimental data points below an equivalence ratio of 0.80 and for all air flow-rates except 270 cc/sec. If the modeling results matched the experimental data perfectly, these ratios would not vary and would give a single number. When the exact match is not achieved the average of the ratios is calculated and used as the conversion factor. The conversion factor is thus based on OH\* chemiluminescence. The conversion

factor is however also applied to  $\text{CH}^*$  chemiluminescence for comparisons because a variation in the conversion factor cannot be justified.

The procedure described above is applied separately to the  $\text{OH}^*$  chemiluminescence results obtained from each of the mechanisms. Due to the separate and independent application of the above procedure, the magnitude of the experimental chemiluminescence data shown varies with the magnitude of the chemiluminescence modeling results.

### **Traditionally accepted $\text{OH}^*$ formation path**

Figure 8.8 compares  $\text{OH}^*$  chemiluminescence yield experimental data and modeling results for all flow-rates and equivalence ratios studied using the traditionally accepted formation path through the  $\text{CH}$  radical. The agreement between model and experiment is limited to low equivalence ratios and low flow-rates. Overall, the features observed in the experimental data are not captured by the model. The location of peak chemiluminescence yield observed in the model varies with flow-rate but always lies on the rich side of the equivalence ratio spectrum, whereas the experimental data shows the chemiluminescence yield peak consistently around an equivalence ratio of 0.90. The modeled  $\text{OH}^*$  chemiluminescence also shows excessive sensitivity to increases in equivalence ratio, especially at higher flow-rates.

### **Formyl radical $\text{OH}^*$ formation path**

Figure 8.9 compares  $\text{OH}^*$  chemiluminescence yield experimental data and modeling results for all flow-rates and equivalence ratios studied using the proposed formation path through the formyl radical. The match obtained between experimental data and modeling results is far superior to that obtained using the traditionally accepted mechanism for  $\text{OH}^*$  formation. The location of peak chemiluminescence yield lies near an equivalence ratio of 0.95 for all flow-rates studied, which agrees well with the experimentally observed peak near an equivalence ratio of 0.90. The match between experimental data and modeling results is particularly good below equivalence ratios of 0.90. The sensitivity of the modeled chemiluminescence yield to

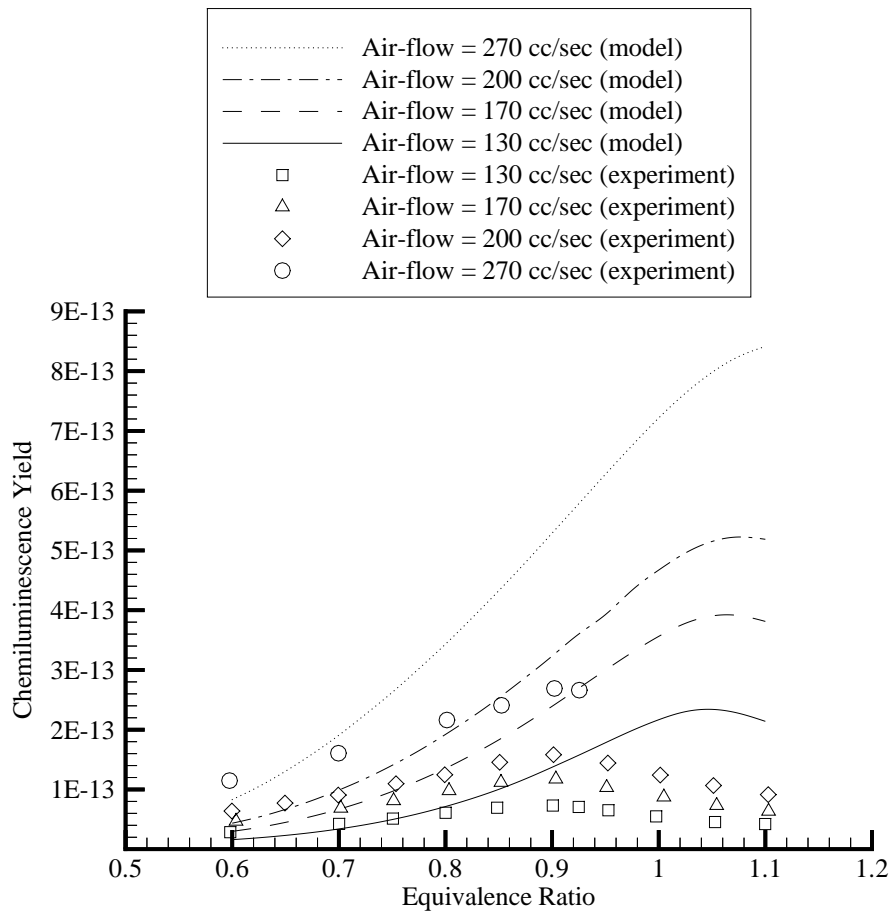


**Figure 8.8:** Comparison between experimental OH\* chemiluminescence data and OH\* chemiluminescence modeling results using the OH\* formation path through CH

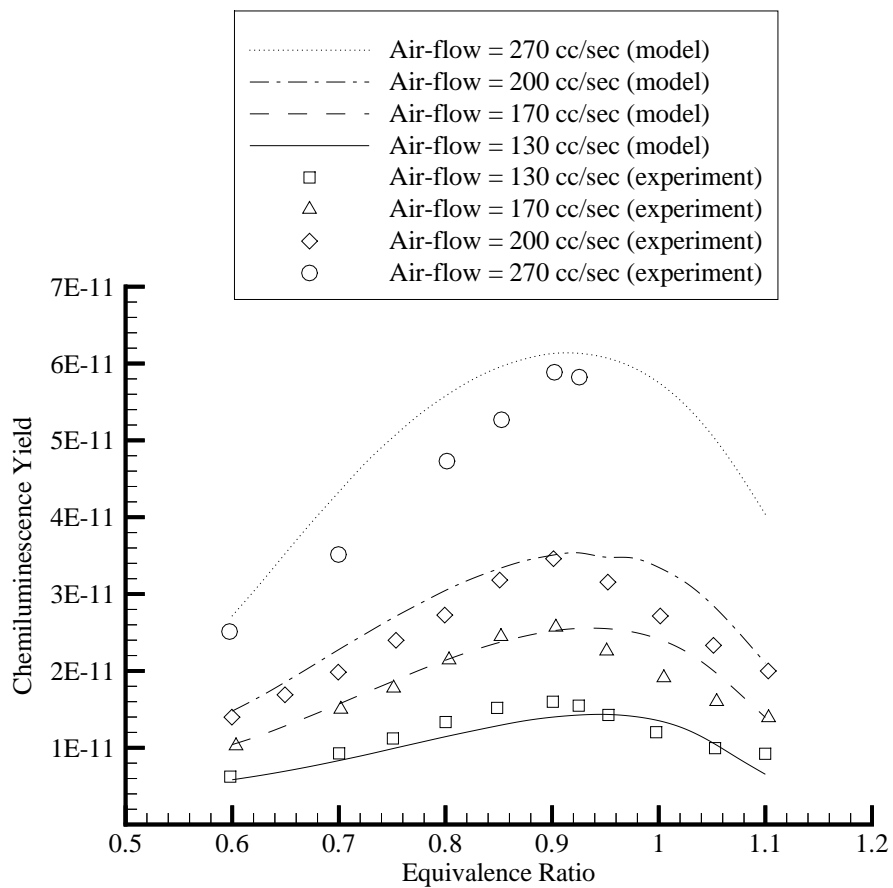
flow-rate is slightly too high, causing slight under-prediction at low flow-rates and over-prediction at high flow-rates. The decrease in chemiluminescence yield with increasing equivalence ratio beyond the maximum yield for the experimental data is steeper than that observed in the modeling results.

Based on these results, it must be concluded that the mechanism using the proposed formation path through the formyl radical is superior to the mechanism using the traditionally accepted formation path in modeling the honeycomb burner. Accordingly all modeling results shown for the remainder of the present chapter are obtained using the mechanism employing the proposed OH\* formation path except where noted explicitly.

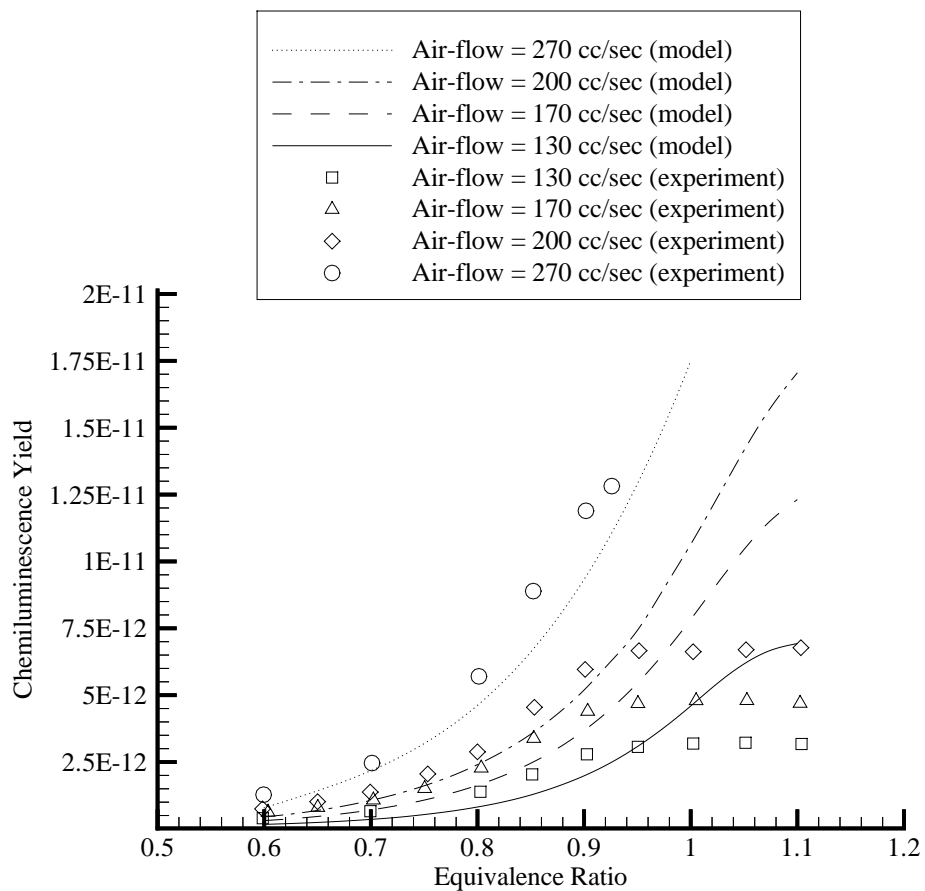
### **CH\* chemiluminescence**

Figure 8.10 compares CH\* chemiluminescence yield experimental data and modeling results for all flow-rates and equivalence ratios studied. Whereas the agreement with experimental data for the Bunsen burner model CH\* results is adequate (see Section 7.4.3), the agreement between experimental data and modeling results is not good for the honeycomb burner. The experimentally observed leveling off of CH\* chemiluminescence yield with equivalence ratio is not seen in the modeling results. The modeling results show a continued strong increase in CH\* yield well beyond the location of the experimentally observed maximum around an equivalence ratio of 1.00. The exponential decrease in CH\* chemiluminescence yield for decreasing equivalence ratios is also observed in the model, but a good match between experimental data and modeling results is still not achieved.

The lack of predictability observed for CH\* chemiluminescence yield makes the development of reliable diagnostics based on CH\* chemiluminescence difficult. The poor match between the predicted CH\* chemiluminescence and the experimental data also makes it difficult to study CH\* as an indicator of heat-release rate using the developed honeycomb model. CH\* chemiluminescence and heat-release rate in the honeycomb burner are discussed in more detail in Section 10.2.2. Possible reasons for the poor match between model and experiment are discussed in Section 9.2.



**Figure 8.9:** Comparison between experimental OH\* chemiluminescence data and OH\* chemiluminescence modeling results using the formation path through HCO



**Figure 8.10:** Comparison between experimental CH\* chemiluminescence data and CH\* chemiluminescence modeling results

## 8.4.2 Gas and Honeycomb temperatures

### Gas temperatures

The results for the gas temperature variation through the entire computational domain are shown in Figure 8.11 and Figure 8.12. Figure 8.11 shows how the axial temperature variation changes under the influence of increasing air flow-rate. The increase in air flow-rate results in an increase in gas temperature throughout the post-flame region. The behaviour of the gas temperature under an increase in flow-rate inside the honeycomb is more complicated due to the competing factors of higher heat output and greater advection. The matter will be discussed further when honeycomb solid temperatures are considered. Outside of the honeycomb, after the flame, the flow-rate increase causes an increase in the gas temperature because of the increased heat released.

The decrease in temperature after the flame is radiation dominated as one can see from the non-linear decrease in the temperature. Note also that the boundary condition used for the gases on the downstream end of the computational domain does not appear to influence the variation of the gas temperature near the boundary, allowing the conclusion that the boundary condition chosen is appropriate.

Figure 8.12 shows the axial variation of the gas temperatures for the entire computational domain for four equivalence ratios. The arrow does not mean to imply that the gas temperatures increase uniformly from an equivalence ratio of 0.9 to 1.10. Rather, the arrow is a way to distinguish the four curves and only indicates that the temperature for the case of an equivalence ratio of 1.10 is greater than the temperature at an equivalence ratio of 0.90. The variation of temperature in the post-flame gases again indicates a radiation dominated energy loss. An interesting difference between the curves shown in Figure 8.12 and Figure 8.11 is the variation in the rate of decrease. Figure 8.12 shows a distinctly higher rate of decrease in temperature for the higher equivalence ratio of 1.10 compared to an equivalence ratio of 0.90. The variation of the rate of decrease is caused by a change in the composition of the the post-flame gases. The richer mixture contains a larger amount of efficient radiators

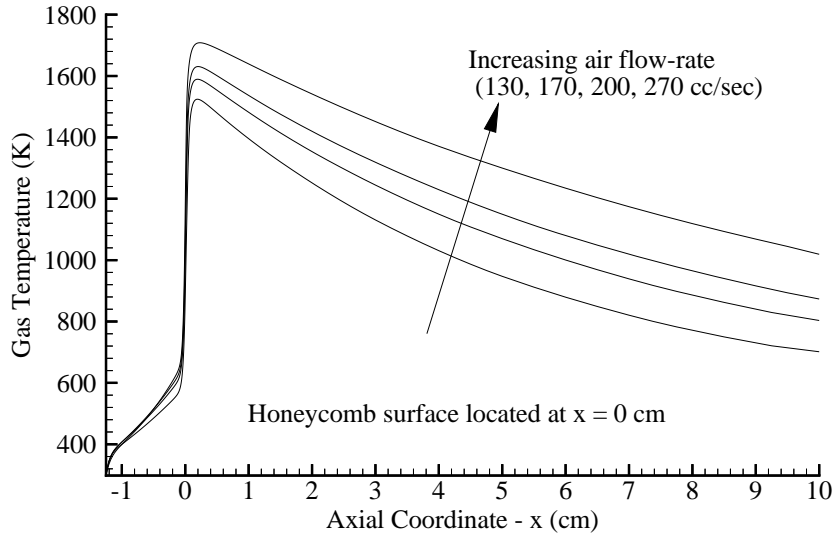


**Figure 8.11:** Computed gas temperatures through the entire computational domain for four flow-rates at an equivalence ratio of 0.75

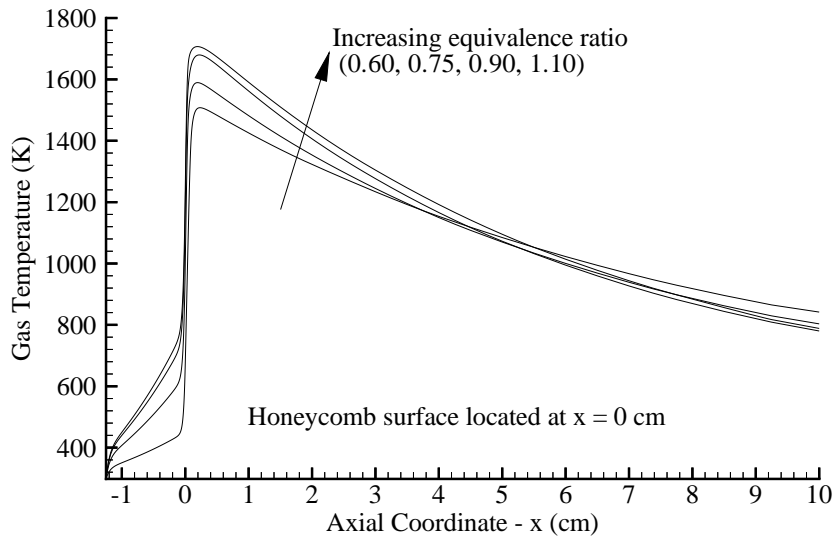
such as water, carbon dioxide and carbon monoxide.

### Honeycomb temperatures

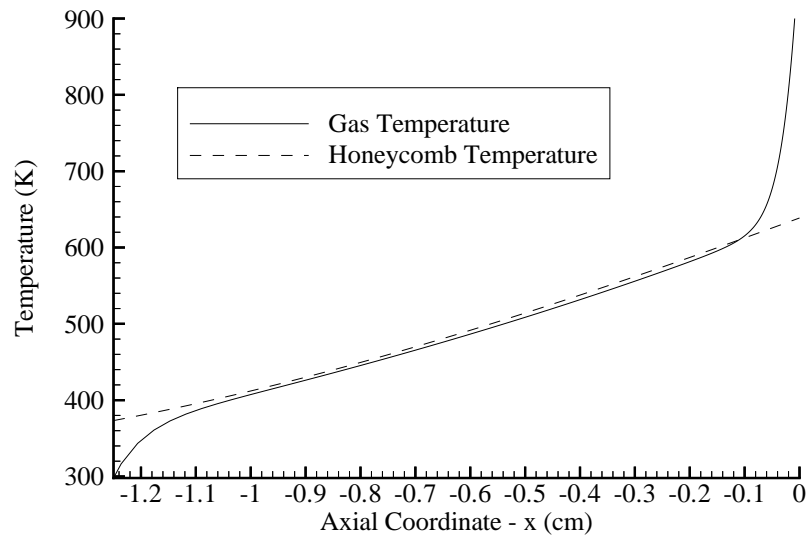
The honeycomb solid temperature variation is shown along with the gas temperature variation inside the honeycomb channel in Figure 8.13. The figure shows clearly how quickly the gas temperature heats up to that of the honeycomb and then remains very closely tied to the honeycomb temperature until the honeycomb exit is approached. The heat transfer between the gas inside the honeycomb channel and the honeycomb channel walls is dominated by the convective mode of heat-transfer.

Figure 8.14 shows how the honeycomb solid temperatures vary as the equivalence ratio is changed. The temperature of the honeycomb increases continuously with the increase in equivalence ratio, similar to the flame temperatures observed in Figure 8.12. The parallel behaviour of honeycomb and flame temperature is not surprising, considering the importance of radiative heat exchange between the flame gases and the honeycomb surface.

The axial variation of honeycomb solid temperatures under changes in air flow-



**Figure 8.12:** Computed gas temperatures through the entire computational domain for four equivalence ratios at an air flow-rate of 170 cc/sec



**Figure 8.13:** Computed honeycomb solid and gas temperatures inside the honeycomb channel at an air flow-rate of 170 cc/sec and an equivalence ratio of 0.75

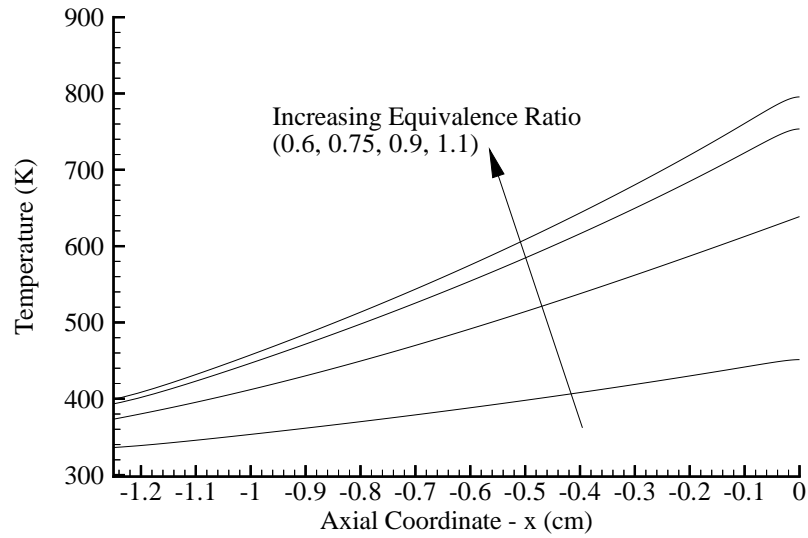


**Figure 8.14:** Computed honeycomb solid temperatures for four equivalence ratios at an air flow-rate of 170 cc/sec

rate is shown in Figure 8.15. The simple trend observed for the post-flame gas temperatures in Figure 8.11 is not found for the honeycomb solid temperatures. Advection and higher honeycomb heat input compete to generate the variation seen in Figure 8.15. As the air flow-rate increases, the flame temperature increases and generates a higher radiative heat flux to the honeycomb surface. At the same time, the residence time of the gas inside the honeycomb is reduced and the rate of temperature increase of the gas is lower. All of these factors combine to cause an actual decrease in the honeycomb inlet temperature for an increase in flow-rate. The temperature increase observed in the model was also verified experimentally, using 0.001 inch thermocouples which were embedded into the honeycomb surface ceramic. (Khanna et al., 2000)

### 8.4.3 Flame location

In experiments, the flame lies just outside the honeycomb for weak flames with equivalence ratios lower than 0.75. Above an equivalence ratio of 0.75, the flame is not able to be distinguished from the red glow of the honeycomb. The model shows

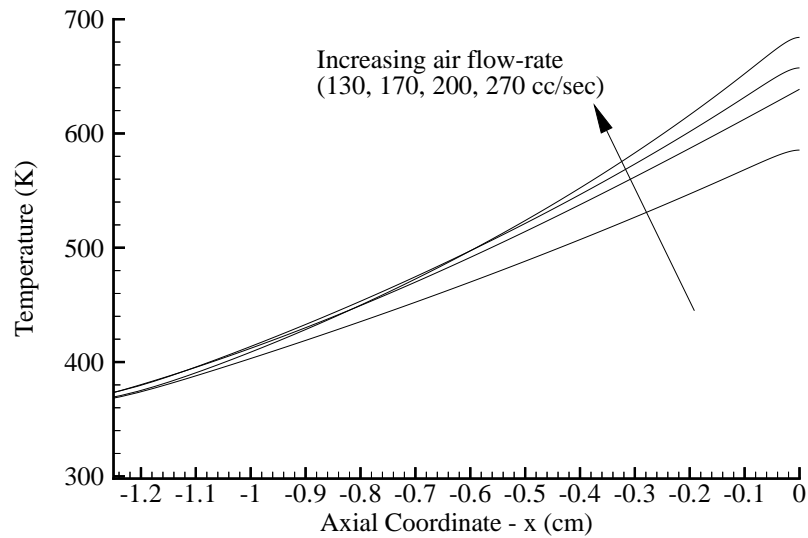


**Figure 8.15:** Computed honeycomb solid temperatures for four air flow-rates at an equivalence ratio of 0.75

similar behaviour. Figure 8.16 shows the flame location at an equivalence ratio of 0.75 for four air flow-rates. The figure shows that the flame sits very close to the honeycomb channel exit. As the flow-rate increases the flame moves closer to the burner exit and slightly into the honeycomb channel. The movement corresponds to a balance between heat-loss and reaction rate. When the burner flow-rate is increased, the reaction rate must increase since the nature of the burner is such that there can be no increase in flame area. The increase in reaction rate is accompanied by an increase in the flame temperature. An increase in the flame temperature in turn causes more radiative heat transfer to the honeycomb solid burner. Not all of the heat transferred to the burner via radiation is lost. Some of the heat is returned to the gas in convective heat transfer. It is the energy return mechanism that causes the flame to move closer to the honeycomb burner when the flow rate is increased. For an overall activation temperature of 16000 °K, a base temperature of 1800 °K and a required increase in the reaction rate of 30%, the increase in flame temperature only has to be about 3%. A 3% increase in the flame temperature results only in a 13% increase in radiation heat-loss. The radiation heat-loss is thus relatively lower at a

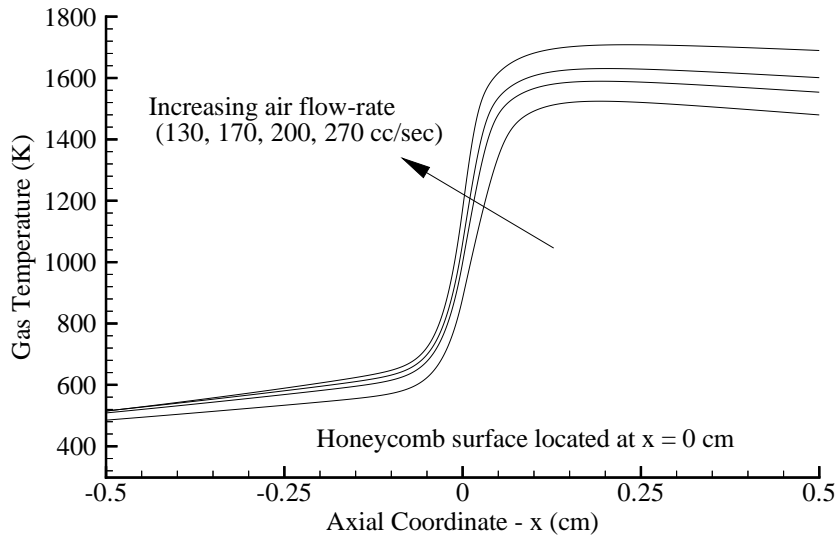


**Figure 8.16:** Computed gas temperatures in vicinity of flame at an equivalence ratio of 0.75 for four air flow-rates

higher burner flow-rate and the flame is forced to move closer to increase heat-loss further.

Figure 8.17 shows how the flame location varies with changes in the mixture equivalence ratio. The flame location changes significantly from an equivalence ratio of 0.60 to an equivalence ratio of 0.75. The flame movement when the equivalence ratio is changed from 0.75 to 0.90 is much smaller than that observed between an equivalence ratio of 0.60 and 0.75. The dependence of the flame location on equivalence ratio reflects the coupling between the flame temperature and flame location but also the non-linear nature of the radiation dominated coupling. Whereas the flame temperature increases are about uniform in changing the equivalence ratio from 0.60 to 0.90, the flame location movement varies vastly depending on the interval of equivalence ratio change considered.

#### 8.4.4 OH\* and CH\* chemiluminescence

Figure 8.18 shows the axial variation of the gas temperature and the chemiluminescent species mole fractions in the vicinity of flame for an air flow-rate of 130 cc/sec

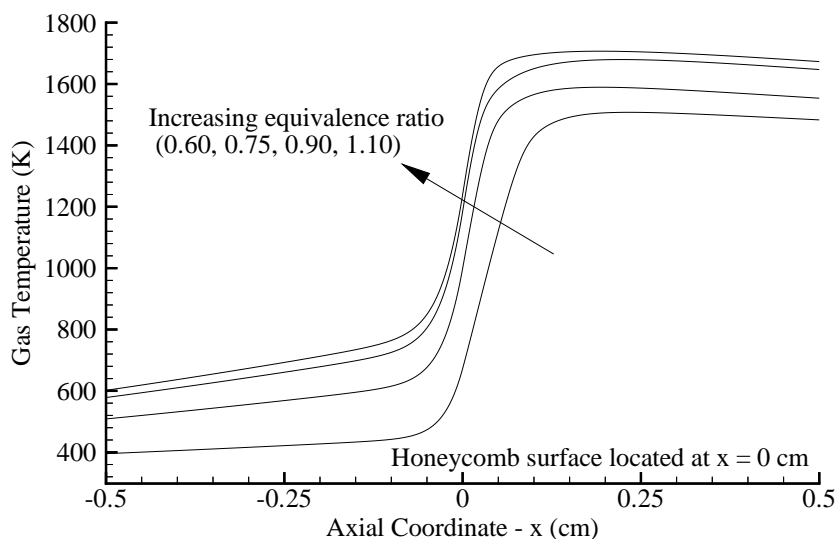


**Figure 8.17:** Computed gas temperatures in vicinity of flame at an air flow-rate of 170 cc/sec for four equivalence ratios

and an equivalence ratio of 1.10. The figure shows that both types of chemiluminescent molecules studied do not occur inside the honeycomb burner and have their peak concentrations near the maximum gas temperature. The  $\text{CH}^*$  mole fraction peak occurs slightly later in the reaction process than the  $\text{OH}^*$  mole fraction peak. Note that the order of magnitude of the mole fraction is very low which is an indication of the truly secondary importance of these species in terms of the overall reaction progress.

### $\text{OH}^*$ chemiluminescence

The lack of direct participation of chemiluminescent species in the reaction process does not diminish their role as one of the few extrinsic indicators closely tied to the combustion process. Figure 8.19 shows the axial variation of the mole fraction of  $\text{OH}^*$  together with the variation of temperature and the variation of the mole fractions of the  $\text{OH}^*$  precursors  $\text{HCO}$  and  $\text{O}$ . To display all three species, the mole fractions were scaled. The figure indicates that the variation of  $\text{OH}^*$  mole fraction is dominated by its production path because the peak  $\text{OH}^*$  mole fraction lies right

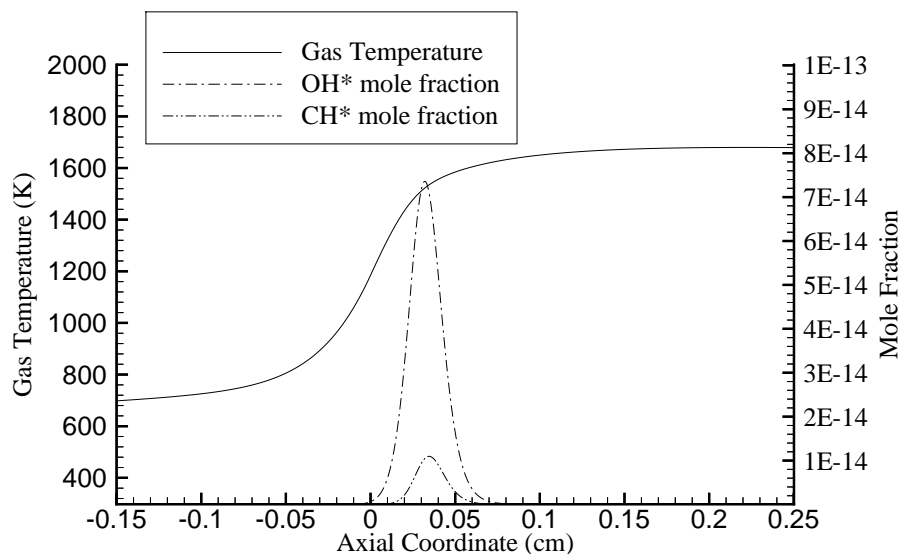


**Figure 8.18:** Computed gas temperatures and chemiluminescent species mole fraction in the vicinity of the flame for an air flow-rate of 170 cc/sec and an equivalence ratio of 0.90

in between the precursor mole fraction peaks. The OH\* mole fraction thus does not appear to be heavily influenced by the availability of different quenching molecules. The quenching process is indeed so much faster that OH\* chemiluminescence can be viewed as a direct indicator of the presence of the two precursor species, the formyl radical and atomic oxygen.

The dependence of OH\* mole fraction on the precursor concentrations can be verified further in Figure 8.20. Figure 8.20 shows the axial variation of the OH\* mole fraction for four equivalence ratios at an air flow-rate of 170 cc/sec. As the equivalence ratio increases, the peaks of the mole fraction move approximately as the flame front does. The magnitude of the peaks however follows the expected trend for a reaction dominated by its formation from the formyl radical and atomic oxygen. Atomic oxygen concentration falls off rapidly for rich mixtures because of the relative abundance of atomic hydrogen. The peak formyl radical concentration also decreases for rich combustion because more carbon conversion occurs through the multi-carbon branch, C<sub>2</sub>H for example. These dependencies on equivalence ratio

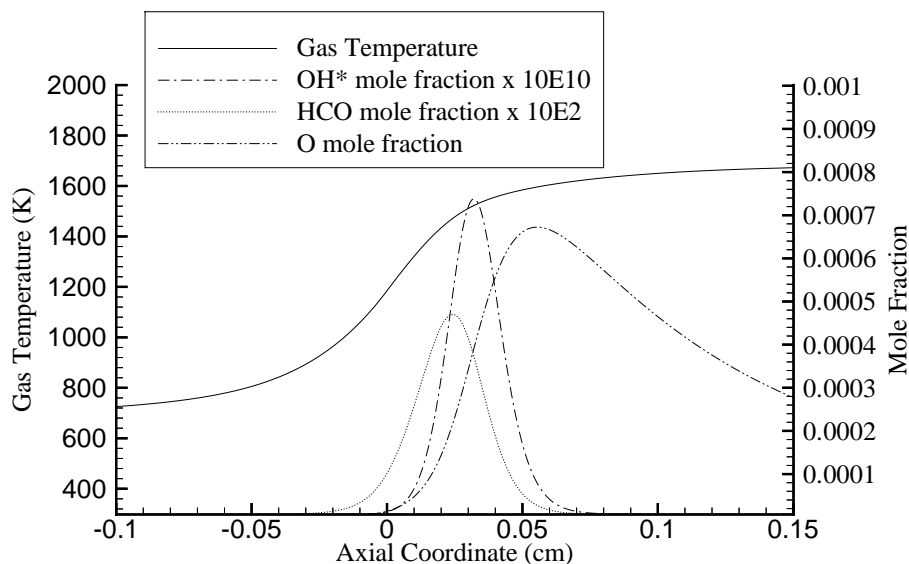


**Figure 8.19:** Computed gas temperatures, OH\*, HCO and O species mole fractions in the vicinity of the flame for an air flow-rate of 170 cc/sec and an equivalence ratio of 0.90

yield the decrease in OH\* chemiluminescence observed from an equivalence ratio of 0.90 to an equivalence ratio of 1.00.

The shifting of the axial variation of OH\* mole fraction for changes in air flow-rate can be observed in Figure 8.21. The figure shows the expected movement with the flame front towards the burner exit as the air flow-rate increases. Due to the increased reaction rate required for the increase in air flow-rate, the peak mole fraction increases steadily as well. The plot confirms the dependence of OH\* chemiluminescence on reaction rate which is the basis for the assumption that chemiluminescence is proportional to heat-release rate.

### CH\* chemiluminescence

Figure 8.22 shows the axial variation of the mole fraction of CH\* together with the variation of temperature and the variation of the mole fractions of the CH\* precursors C<sub>2</sub>H and O. To display all three species the mole fractions were scaled. The figure indicates that the variation of CH\* mole fraction is dominated by its production path

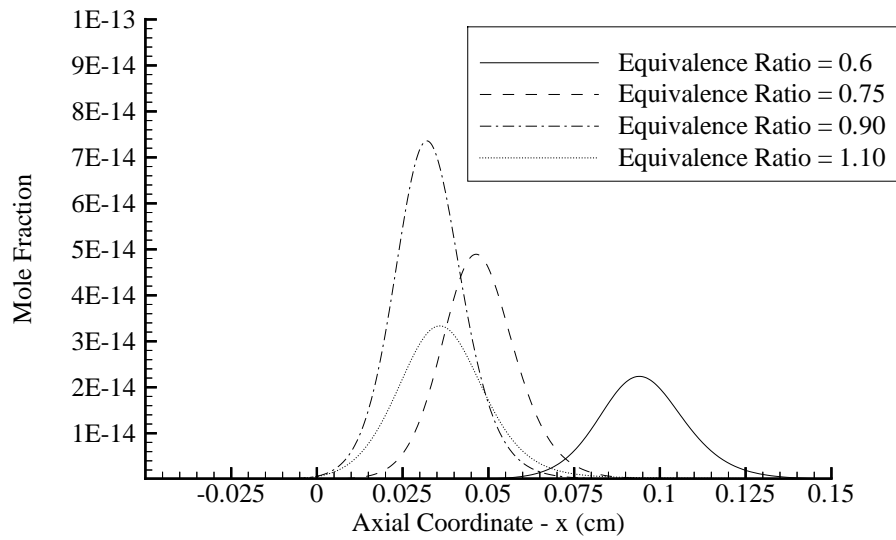


**Figure 8.20:** Computed axial variation of OH\* mole fraction in the vicinity of the flame for four equivalence ratios at an air flow-rate of 170 cc/sec

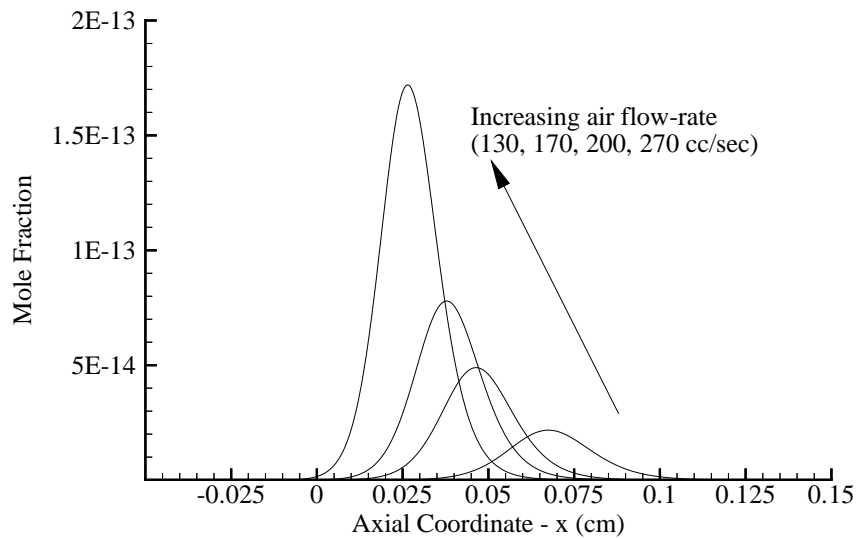


**Figure 8.21:** Computed axial variation of OH\* mole fraction in the vicinity of the flame for four flow-rates at an equivalence ratio of 0.75

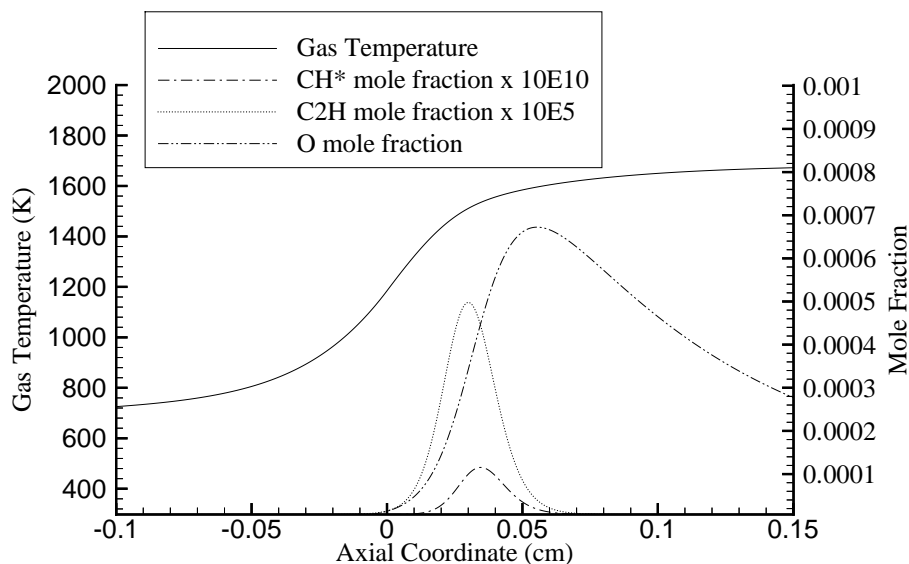


**Figure 8.22:** Computed gas temperatures, CH\* C<sub>2</sub>H and O species mole fractions in the vicinity of the flame for an air flow-rate of 170 cc/sec and an equivalence ratio of 0.75

because the peak CH\* mole fraction lies right in between the precursor mole fraction peaks. The CH\* mole fraction thus does not appear to be heavily influenced by the availability of different quenching molecules. The quenching process is indeed so much faster that CH\* chemiluminescence can be viewed as a direct indicator of the presence of the the two precursor species, the C<sub>2</sub>H radical and atomic oxygen.

The dependence of CH\* mole fraction on the precursor concentrations can be verified further in Figure 8.23. Figure 8.23 shows the axial variation of the CH\* mole fraction for four equivalence ratios at an air flow-rate of 170 cc/sec. As the equivalence ratio increases, the peaks of the mole fraction move approximately as the flame front does. The magnitude of the peaks however follows the expected trend for a reaction dominated by its formation from the C<sub>2</sub>H radical. As discussed above for OH\* chemiluminescence, the atomic oxygen mole fraction decreases significantly even before the stoichiometric point is reached. The CH\* mole fraction peaks still seem to increase exponentially at an equivalence ratio of 1.10, as can also be seen in Figure 8.10. The variation suggests that CH\* formation is most sensitive to the

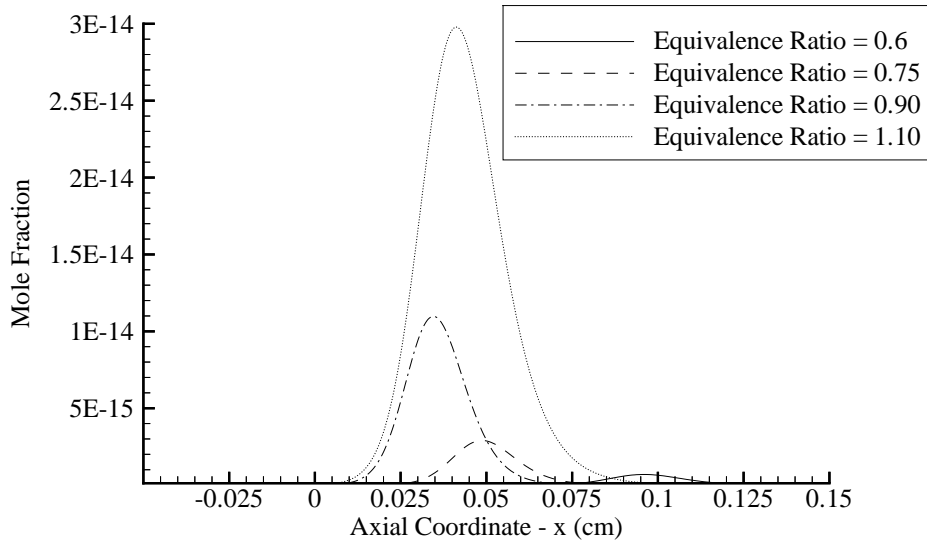


**Figure 8.23:** Computed axial variation of  $\text{CH}^*$  mole fraction in the vicinity of the flame for four equivalence ratios at an air flow-rate of 170 cc/sec

presence of the  $\text{C}_2\text{H}$  radical. The existence of  $\text{C}_2\text{H}$  is so sensitive to equivalence ratio that the decrease of the other participating species in  $\text{CH}^*$  formation, atomic oxygen, does not appear to affect  $\text{CH}^*$  formation significantly. The reason for the high sensitivity of  $\text{CH}^*$  to equivalence ratio lies in the fact that the two carbon branch of fuel conversion becomes much more populated at higher equivalence ratios. The reason discussed above for the decrease in formyl radical production is also responsible for the increase in  $\text{C}_2\text{H}$  radical production and thus for the increase  $\text{CH}^*$  formation.

The shifting of the axial variation of  $\text{CH}^*$  mole fraction for changes in air flow-rate can be observed in Figure 8.24. The figure shows the expected movement with the flame front towards the burner exit as the air flow-rate increases. As observed for  $\text{OH}^*$ , the increased reaction rate required for the increase in air flow-rate causes the  $\text{CH}^*$  mole fraction to increase steadily as well. The plot confirms the dependence of  $\text{CH}^*$  chemiluminescence on reaction rate which is the basis for the assumption that chemiluminescence is proportional to heat-release rate.

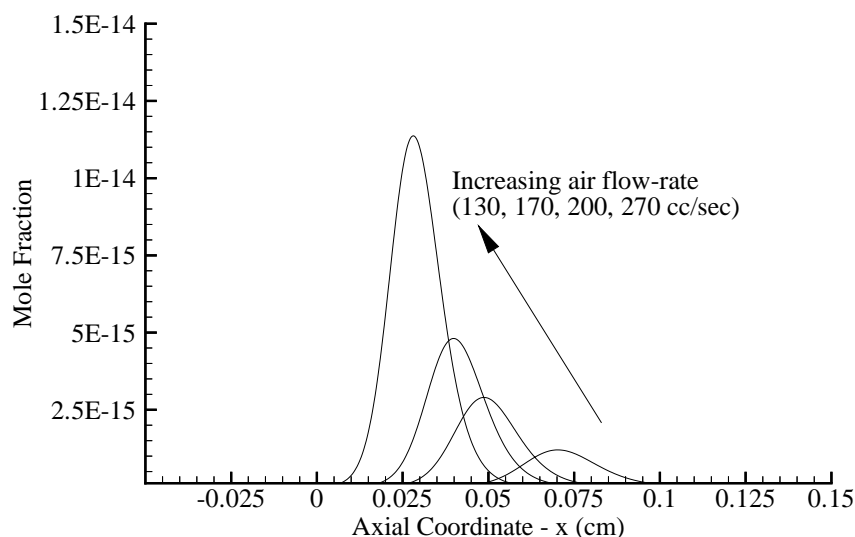


**Figure 8.24:** Computed axial variation of  $\text{CH}^*$  mole fraction in the vicinity of the flame for four air flow-rates at an equivalence ratio of 0.75 cc/sec

### 8.4.5 Unaltered chemical mechanism

In order to ensure that the changes made to the GRIMECH reaction mechanism (Smith et al., 1999), described in Section 6.2.3 do not significantly influence the overall characteristics of the combustion, the  $\text{OH}^*$  mechanism is included in the unmodified GRIMECH mechanism but the  $\text{CH}^*$  reactions are not included. Calculations using the unmodified GRIMECH mechanism with  $\text{OH}^*$  reactions are then compared to the results presented above.

Figure 8.25 shows the difference in percent between the two mechanisms at an air flow-rate of 130 cc/sec and varying equivalence ratio. The difference between the two mechanisms does not exceed 1.5 % and shows little deterministic trend with equivalence ratio. These results show that the modifications made to the mechanism as described in Section 6.2.3 do not affect the overall behaviour of the flame significantly. The results underline the fact that detailed chemical mechanisms do not improve the prediction of global flame characteristics but rather allow the modeling of intermediate species that may not contribute significantly to the characteristics of

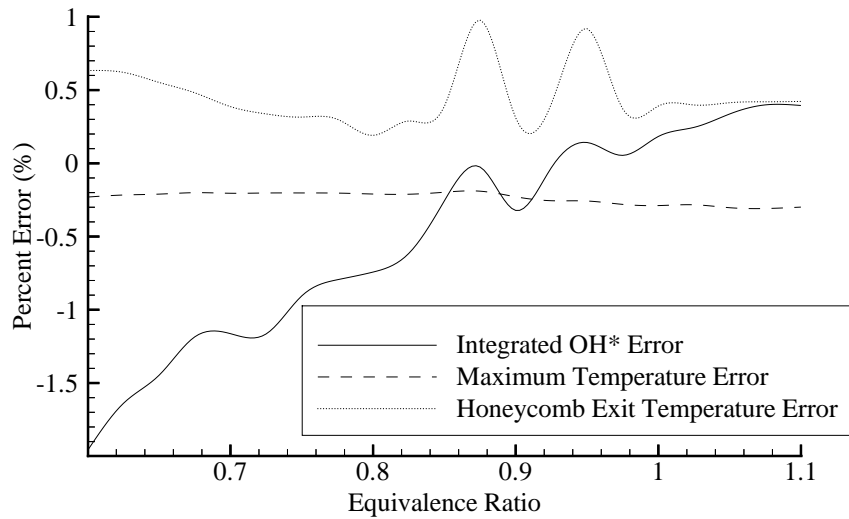


**Figure 8.25:** Variation of the difference between the altered chemical mechanism and the original GRIMECH chemical mechanism with OH\* reactions with equivalence ratio for an air flow-rate of 130 cc/sec

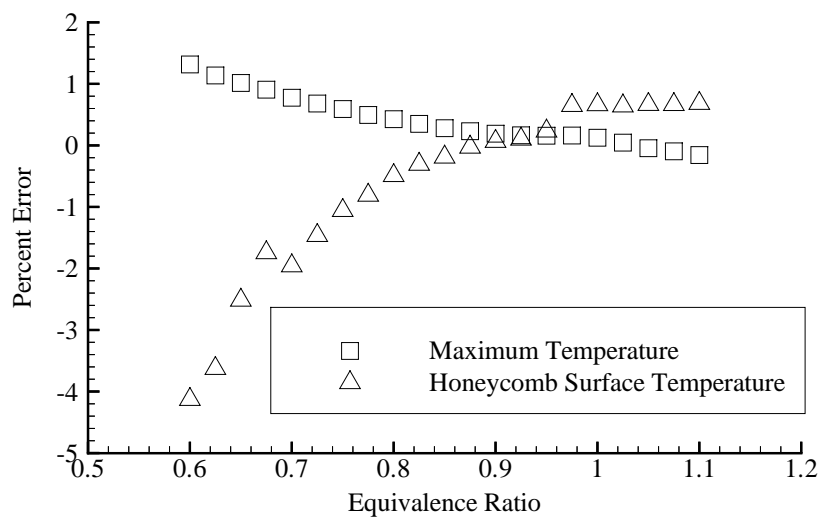
the flame.

#### 8.4.6 Small chemical mechanism

To study the possibility of decreasing the computational time of the honeycomb model, a reduced chemical mechanism taken from Smooke, M.D. (1991) is modified by adding the equations governing OH\* production and consumption. The mechanism only contains 25 reactions and computational time for the model therefore was reduced by an order of magnitude.

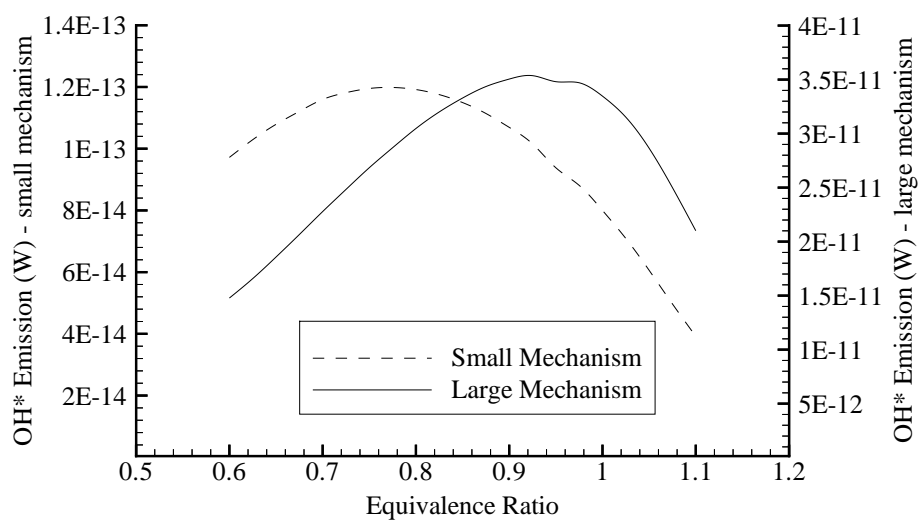
To form the comparison, the model calculations are repeated using an air flow-rate of 200 cc/sec and equivalence ratios in the range from 0.60 to 1.10. As shown in Figure 8.26, the reduced mechanism matches the results of the large mechanism for honeycomb surface temperature and maximum gas temperature very well.

Figure 8.27 contrasts the results of each chemical mechanism for OH\* chemiluminescence production. The figure shows that neither the magnitude nor the overall behaviour of the calculated OH\* chemiluminescence emission from the reduced chem-



**Figure 8.26:** Variation of the difference between the reduced chemical mechanism (Smooke, 1991) and the modified GRIMECH 3.0 mechanism with equivalence ratio for an air flow-rate of 200 cc/sec

ical mechanism matches the large chemical mechanism results. The results underline the fact that large chemical reaction mechanisms are needed to predict intermediate species profiles correctly and that small reduced order mechanisms are designed to give accurate temperature distributions. It may be possible to adapt the reduced chemical mechanism to give accurate OH\* chemiluminescence emission results, but such a study is outside the scope of the present work.



**Figure 8.27:** OH\* chemiluminescence emissions predicted by the reduced and large chemical mechanism at an air flow-rate of 200 cc/sec for varying equivalence ratio